PCCP

PAPER

View Article Online
View Journal | View Issue

Cite this: *Phys. Chem. Chem. Phys.*, 2017, **19**, 31168

Self-assembly of $(WO_3)_3$ clusters on a highly oriented pyrolytic graphite surface and nanowire formation: a combined experimental and theoretical study

Xin Tang,[a] Kit H. Bowen*[a] and Florent Calvo*[b]

Received 22nd July 2017,
Accepted 21st October 2017

DOI: 10.1039/c7cp04952h

rsc.li/pccp

Tungsten oxide cluster anions $(WO_3)_3^-$ produced from a magnetron source were soft-landed on highly oriented pyrolytic graphite (HOPG) surfaces at different temperatures, and the structures formed upon deposition were analyzed using *ex situ* atomic force microscopy. Under liquid nitrogen cooling conditions of 100 K, the clusters form small branched nanostructures extending over a few nanometers with a height not exceeding 1 nm. At 673 K, nanowires approximately 100 nm long and less than 10 nm in diameter are observed. Dedicated atomistic modeling of the early steps of the assembly process was carried out using a polarizable potential parametrized to reproduce electronic structure calculations on small clusters, and accounting for the corrugated interaction with the ideal HOPG surface. Molecular dynamics simulations reproduce the branched nanostructures formed at low temperature fairly well, and confirm the loss of ramification at higher temperatures. Additional simulations of coalescence processes between nanoislands containing a hundred $(WO_3)_3$ units produce elongated shapes as observed experimentally, providing a typical size of the individual building blocks. The preferred orientation of nanowires and additional *in situ* X-ray photoelectron spectra both further suggest that the nanostructures grow along terraces and could bind through chemical processes and possibly tungsten carbide formation.

1 Introduction

Metal oxide clusters and nanoparticles are of great interest owing to various applications in catalysis and materials science.[1] In order to utilize metal oxide clusters, usually, they have to be dispersed into solutions or adsorbed onto an underlying support. For the latter case, the interaction between oxide clusters and the supports becomes critically important, since it can modify both their geometric and electronic structures. It has become well known that the surface defects, functional groups, and electronic properties of the support can alter the structure of the clusters.[2–4] Therefore, understanding the details of the interactions and dynamic processes leading to these structures can have a significant impact on the application of metal oxide clusters.

Tungsten oxide trimer clusters, *i.e.* $(WO_3)_3$, have been well studied among many oxide clusters because they are a major sublimation product of tungsten oxides. The geometric and electronic structures of gas phase $(WO_3)_3^-$ clusters have been experimentally and theoretically characterized by Wang *et al.*, who suggested a six-member ring structure,[5] which was subsequently confirmed by scanning tunneling microscopy (STM) measurements for $(WO_3)_3$ clusters on $TiO_2(110)$.[6] Furthermore, using $(WO_3)_3/TiO_2(110)$ as a model system, Donalek *et al.* have shown that $(WO_3)_3$ clusters on TiO_2 exhibit rich catalytic activity toward alcohol dehydration,[7] dehydrogenation and formaldehyde polymerization reactions.[8] The interactions between $(WO_3)_3$ clusters with other supports have also been studied experimentally and theoretically, and many interesting structures have been found. For example, on the FeO(111)/Pt(111)[9] and Cu(110) surfaces,[10] two-dimensional tungstate structures were observed *via* STM. On the Pt(111) surface, a compact layer of $(WO_3)_3$ clusters was formed under thermal treatment.[11] All these studies underlined that $(WO_3)_3$ can be used as a versatile model cluster to study both the cluster–cluster and cluster–surface interactions.

In the present investigation, the surface assembling behaviors of $(WO_3)_3$ clusters on highly oriented pyrolytic graphite (HOPG) were studied as a function of surface temperature and coverage by both atomic force microscopy (AFM) and computational modeling based on molecular dynamics (MD) simulations at

[a] *Department of Chemistry, Johns Hopkins University, Baltimore, MD 21218, USA. E-mail: kbowen@jhu.edu*
[b] *Univ. Grenoble Alpes, LIPHY, F-38000 Grenoble, France and CNRS, LiPhy, F-38000 Grenoble, France. E-mail: florent.calvo@univ-grenoble-alpes.fr*

the atomistic level of detail, assuming an ideal HOPG substrate. HOPG surfaces are often employed as substrates to support nanoparticles and nanoclusters because they are atomically smooth, chemically inert, and easy to prepare.[12–16] Compared to non-conductive substrates such as SiO_2, the HOPG substrate can neutralize the charged particles and thus allow them to be deposited on the surface by avoiding surface charging. The $(WO_3)_3$ cluster was chosen as a model system to study the cluster–cluster and cluster–surface interactions. The immediate application of such a study is to help the design of single site catalysts,[17–20] which are essentially isolated clusters, *i.e.*, monomers or oligomers supported on various surfaces dominated by cluster–surface interactions. Additionally, a better understanding of cluster–cluster interactions will benefit the building of cluster-assembled materials.[21]

The simulations generally reproduce the trends observed in the measurements, with the formation of dendritic nanostructures at low temperature revealing diffusion-limited aggregation (DLA) processes. At higher temperature, our simulations produce coarser nanostructures that are of comparable dimension to the experimentally observed nanowires, suggesting a typical size for these systems. However, in the absence of surface defects or surface reactions on terraces, our modeling is unable to account for the preferential orientation of nanowires along crystallographic directions. The importance of the reactions is confirmed by additional X-ray photoelectron spectroscopy measurements, which suggest the formation of tungsten carbide and more generally chemical reactions that pin down the nanostructures to the carbon substrate much more strongly than our computational model can account for.

The experimental and computational methods are given in Section 2, with our results being presented and discussed in Section 3. Concluding remarks are finally given in Section 4.

2 Methods

2.1 Experimental methods

Tungsten oxide cluster anions were produced using a magnetron sputtering source and mass selected by passing through a magnetic sector mass spectrometer before being soft-landed onto a HOPG surface. The apparatus for cluster deposition has been described in detail elsewhere.[22] Tungsten oxide cluster anions were created in the magnetron ion source by reactive sputtering of a tungsten metal target in the presence of oxygen with a partial pressure of 0.2–0.3 mbar. Once produced, they were then accelerated to 1500 V before entering a magnetic sector mass spectrometer (25° sector magnet with a resolution of $m/\Delta m = 20$). By adjusting the strength of the magnetic field, we were able to mass-select $(WO_3)_3^-$ cluster anions. After refocusing and collimating by a series of ion optics, the size-selected $(WO_3)_3^-$ cluster anions were decelerated to kinetic energies of less than 0.1 eV per atom and soft-landed onto a freshly cleaved HOPG substrate without applying any bias voltage. The target was cooled to liquid nitrogen temperature and heated by passing current through it. Two significantly different deposition temperatures, *i.e.* 100 K and 673 K, were chosen to examine the cluster–cluster interaction and cluster–surface interaction in a wide temperature window. These two temperatures are limited by the cooling and heating capability of the sample holder. The pressure during cluster deposition was typically $\sim 10^{-9}$ mbar.

To characterize the surface structures of the deposited clusters, *ex situ* AFM was used assuming no surface morphology changed during air exposure. It should be noted that in our previous studies[23] on molybdenum oxide clusters supported on HOPG, both *in situ* and *ex situ* characterizations of metal oxides exhibited consistent chemical compositions of metal oxides. AFM images were acquired as a function of increasing cluster coverage, employing a PicoSPM LE AFM (Agilent Technologies) operated in magnetic tapping mode using Co-Cr tips obtained from MikroMasch (NSC18). All image rendering and height measurements were performed with commercially available software from Agilent Technologies. The chemical composition of the deposited clusters was determined using *in situ* XPS, where the sample can be directly transferred to an adjunct XPS analysis chamber without exposure to air. This was achieved with a PHI 5400 XPS system equipped with a Mg Kα X-ray source (1253.6 eV). XP spectra were processed with commercially available software (CasaXPS). Peak positions in the spectra were referenced to the C(1s) graphite peak (284.5 eV) of the HOPG substrate, and metal oxidation states were fit using mixed Gaussian (30%)/Lorentzian (70%) envelopes.

2.2 Computational modeling

In addition to experimental measurements, we have carried out atomistic simulations of the nanostructures grown by successive addition of $(WO_3)_3$ units on HOPG at fixed temperature. Approaches using an explicit description of electronic structure such as density-functional theory are not practical to address the dynamics of nanostructures containing hundreds of atoms, neither are fully coarse-grained methods treating individual tungsten oxide trimers as rigid owing to their possible rearrangement upon deposition and growth. We thus employ an intermediate level description using a many-body polarizable potential that captures the essential physical and chemical ingredients of the interactions between tungsten and oxide ions in the presence of the ideal HOPG substrate.

Our computational approach follows the lines of our earlier work on deposited magnesium oxide clusters[24] and relies on a polarizable many-body potential that takes into account the corrugation and dielectric nature of the graphite substrate. A fluctuating-charges model originally developed for bare magnesium oxide clusters[25] was extended to treat tungsten oxide clusters. This model naturally incorporates the mixed ionic–covalent nature of the oxide bonds, and allows the partial charges carried by the ions to depend on their local coordination. The charges are not defined *a priori* but are obtained self-consistently to achieve electronegativity equalization for each atomic configuration. Briefly, the total interaction potential V depends on the instantaneous atomic configuration $\mathbf{R} = \{r_{ij}\}$ of the ions through a repulsive pairwise potential taken as a Born–Mayer form $V_{\mathrm{rep}}(r_{ij}) = D_{ij}\exp(-b_{ij}r_{ij})$,

where r_{ij} is the distance between ions i and j, D_{ij} and b_{ij} are two parameters, and the electrostatic contribution $V_Q(\mathbf{R})$ is cast as

$$V_Q(\mathbf{R}) = \sum_i \left[\eta_i q_i + \frac{1}{2}U_{ii}^0 q_i^2 - \frac{1}{2}\alpha_i \boldsymbol{E}_i^2\right] + \sum_{i<j} J_{ij}(r_{ij}) q_i q_j + \lambda\left(Q - \sum_i q_i\right) \quad (1)$$

In this equation, q_i is the charge carried by ion i, η_i denotes the electronegativity of the corresponding element, U_{ii}^0 its hardness and α_i its isotropic atomic polarizability, and J_{ij} the Coulomb integral between ions i and j, which is approximated in the Ohno representation[26] as

$$J_{ij}(r) = \frac{1}{\left[r^2 + \left(U_{ii}^0\right)^{-2}\exp\left(-\gamma_{ij} r^2\right)\right]^{1/2}} \quad (2)$$

and thus involves one additional damping parameter γ_{ij}. In eqn (1) the electric field vector $\boldsymbol{E}_i$ on ion i is defined consistently with the Coulomb interaction J_{ij} as

$$\boldsymbol{E}_i = \sum_{j\neq i} -q_j \frac{\partial J_{ij}}{\partial r_i} \quad (3)$$

Finally, the last term of eqn (1) constrains the total charge of the system to equal the value Q with λ being a Lagrange multiplier. Q is taken to be 0 throughout this work, assuming that upon deposition, the tungsten oxide trimer anions release their electron into the substrate and become neutralized.

In the absence of surface defects and surface reactions, the ideal HOPG substrate interacts with deposited tungsten oxide clusters through weak repulsion–dispersion forces that can be modeled using the well-established Steele potential.[27] However, because the graphite surface is highly polarizable, it is important to also describe correctly the electrostatic contribution in the presence of image charges and their influence on the fluctuating charges potential.

The repulsion–dispersion energy $V_{HOPG}(\mathbf{r})$ accounts for the lateral corrugation of graphite *via* periodic functions in the corresponding dimensions.[24] The first terms in the Fourier expansion of $V_{HOPG}(\mathbf{r})$ result from the integration of the Lennard-Jones potential on the multilayer graphitic substrate and read:

$$V_{HOPG} = V_0(z_i) + V_1(z_i) f_1(x_i,y_i) + V_2(z_i) f_2(x_i,y_i) \quad (4)$$

in which the functions $f_k(x_i,y_i)$ denote the first harmonics along the lateral dimensions x and y[24,27] and the functions $V_k(z)$ are chosen similarly as in our previous paper.[24] In particular, instead of the cumbersome expressions for V_1 and V_2 involving Bessel functions of the second kind, more practical numerical forms were employed as

$$V_k(z) \simeq \chi_k \frac{\exp(-\beta_k z)}{z_k^{\rho_k}} \quad (5)$$

The parameters entering this last expression were numerically adjusted from the exact expressions for the functions V_k, using the Lennard-Jones parameters appropriate for the W–C and O–C interactions, as taken from the OPLS force field.[28]

The HOPG substrate is also strongly polarizable and ions in contact interact with their image charges. The additional electrostatic and polarization energies originating from this interaction between the ions and the substrate were modeled as already achieved for MgO clusters, distinguishing the responses of the electric field in the parallel and perpendicular directions to the surface as:[29]

$$V_{\parallel}(\mathbf{R}) = -\sum_i \left[\frac{q_i^2}{4z_i} - \frac{1}{2}\sum_{j\neq i}\frac{q_i q_j}{r_{ij}'}\right] \quad (6)$$

$$V_{\perp}(\mathbf{R}) = -\sum_i \left[\frac{2\pi\alpha_{\perp} q_i^2}{8z_i^2} - \frac{1}{2}\sum_{j\neq i}\frac{2\pi\alpha_{\perp} q_i q_j (z_i + z_j)}{\left(r_{ij}'\right)^3}\right] \quad (7)$$

In these equations, z_i is the distance from ion i to the substrate and r_{ij}' is the distance between ion i and the image charge of ion j on the other side of the HOPG surface, $\alpha_{\perp} = 0.220$ Å is the polarizability density of the graphite surface.[30] Given the linear dependence of the electric field $\boldsymbol{E}_i$, these additional terms combine with V_Q above to yield a quadratic expression as a function of q_i, which can be minimized exactly by linear algebra techniques, or in molecular dynamics using extended Lagrangian techniques.[31,32]

The above potential was parametrized against recent quantum chemical calculations performed by Li and Dixon on isolated $(WO_3)_n$ clusters,[32] for which equilibrium geometries, energy differences between isomers and even partial charges on ions were provided, as obtained from a natural bond orbital analysis. The final values for the parameters are listed in Table 1 together with the parameters for the cluster–HOPG interaction.

This potential above was employed to simulate the growth and annealing of clusters of $(WO_3)_3$ units on the HOPG substrate, using several approximations designed to make systems containing thousands of atoms tractable. As previously used for MgO clusters on HOPG,[24] a two-step procedure was employed to grow assemblies sequentially by addition of a single building block on a fixed seed $[(WO_3)_3]_n$, both collision partners being treated as rigid during the approach before the product $[(WO_3)_3]_{n+1}$ is fully relaxed without the rigid constraints. For each iteration n,

Table 1 Parameters of the many-body potential, all expressed in atomic units

Parameter	W	O	W–O
D	49.74	32.50	17.97
b	1.46	2.05	1.61
U	1.41	0.77	2.82
η	−2.61	0	
α	0.073	1.56	
χ_1	16436.6	319035.5	
χ_2	1 983 271	1 003 294	
ρ_1	0.105	0.137	
ρ_2	1.06×10^{-7}	0.364	
β_1	2.983	2.966	
β_2	4.189	3.935	
σ	5.940	1.091×10^{-4}	
ε	6.304	1.03×10^{-4}	

the relative orientations of the two partners were chosen randomly and an impact parameter b was drawn from the normalised distribution $p(b) = b/b_{max}$, where b_{max} equals the sum of the gyration radii of the two partners. The $(WO_3)_3$ projectile was thrown at the existing assembly with a fixed kinetic energy of 100 K or 600 K depending on the growth conditions. Each MD trajectory assuming rigid collision partners was propagated until the distance between them came to below 5 Å, at which stage a smooth fluid damping force was introduced to stop the projectile. A maximum duration of 100 ps was imposed in the (rare) situations where the projectile did not meet the target, in which case another collision trajectory was restarted. In practice, the velocity was reduced by 0.01% every time step of 1 fs after the contact was established as a way to mimic the dissipation of translational kinetic energy into the vibration modes of both partners and the substrate, which in our model, is only implicit and cannot dissipate the excess energy of the nucleation process taking place between the ionic clusters. Once the projectile had stopped, the partial charges of all atoms were calculated by minimizing the electrostatic contribution to the potential, and all atomic positions of the coalesced nanostructure were locally optimized before sending a new building block toward the existing assembly.

3 Results and discussion

AFM images of $(WO_3)_3$ trimer clusters deposited at 100 K are shown in Fig. 1 with increasing coverage [panels (a)–(c)]. Upon deposition onto the HOPG surface, at low coverage, $(WO_3)_3$ clusters grow into small fractal-like structures with an average height of 0.7 nm, indicative of two-dimensional aggregation. With increasing coverage, the HOPG surface is more populated with tungsten oxide clusters until a full monolayer of tungsten oxide is achieved. After the surface was annealed to 673 K [panels (d)–(f) in Fig. 1], AFM examination does not reveal dramatic changes in the surface structures of the clusters, which suggests a strong interaction between oxide clusters and the underlying graphite surface. It has to be noted that at higher coverage, the structures after the annealing show some preferential orientation of the aggregates, indicating a stronger interaction between oxides and the substrate at elevated temperatures.

In contrast, deposition of $(WO_3)_3$ clusters on HOPG at 673 K produces one-dimensional nanowire structures approximately 100 nm long, as shown in Fig. 2, which have not been previously observed. These nanowires are usually oriented at a specific angle to each other, *i.e.* 60° or 120°, further supporting the strong nature of the interaction between $(WO_3)_3$ clusters and the underlying graphite substrate under elevated temperatures. In addition to the nanowire structures observed here, small aggregates of tungsten oxide trimers are also found. It is known that small clusters prefer to aggregate on step edges and grain boundaries to form nanowire/nanoarray structures upon deposition onto graphite surfaces.[33,34] This is due to their high mobility on HOPG terraces and also the higher affinity of surface line or point defects. In the present case of $(WO_3)_3$ clusters deposited on HOPG at 673 K, the particularly long nanowires observed with

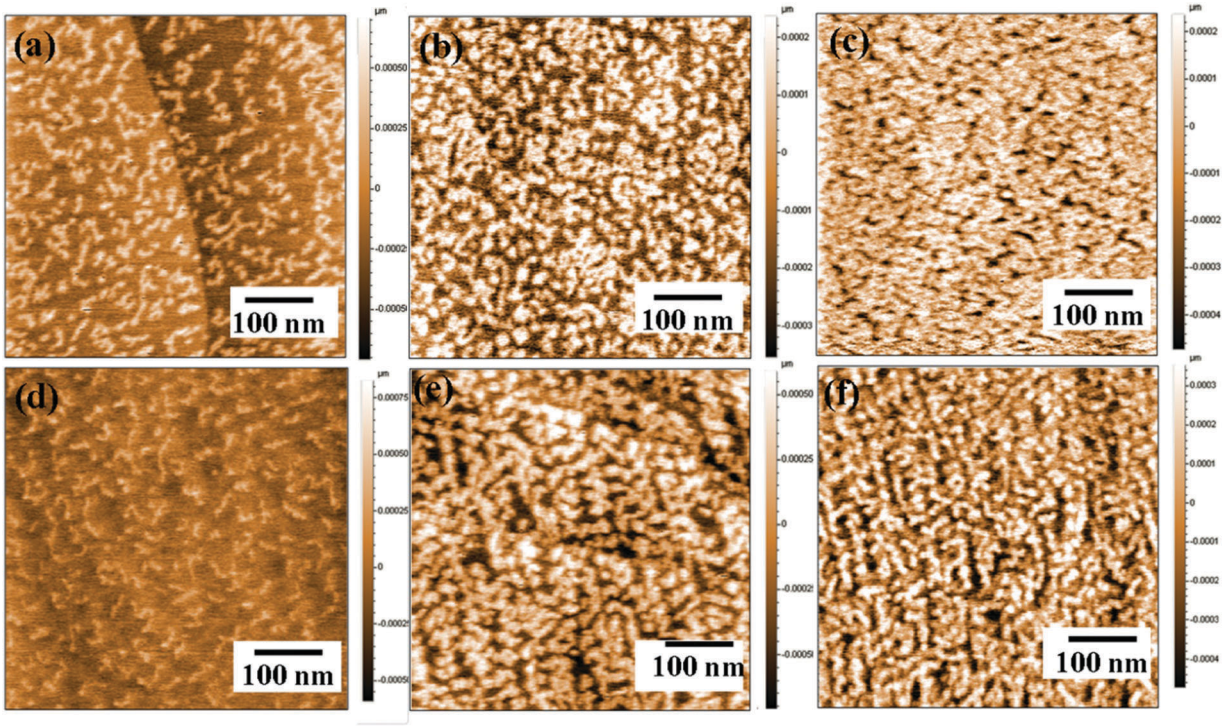

Fig. 1 AFM Images of deposited $(WO_3)_3$ clusters as deposited at 100 K with coverage increasing from (a)–(c) and after annealing at 673 K with coverage increasing from (d)–(f). (The average coverage corresponds to 4.8 W nm^{-2}, where the lower coverage images are taken from regions near the edge of the beam.)

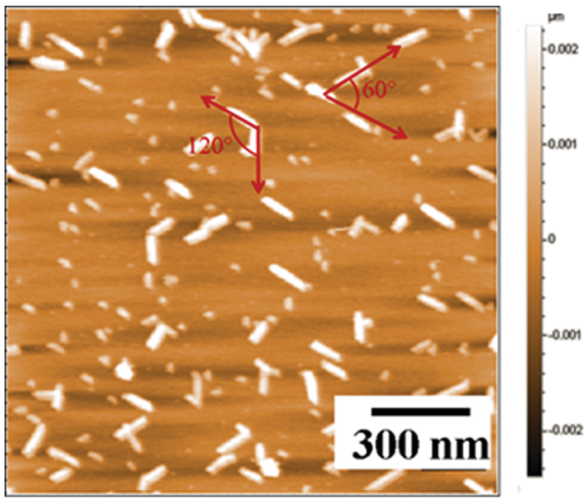

Fig. 2 AFM Images of $(WO_3)_3$ clusters as deposited at 673 K.

AFM probably originate from nucleation along terraces due to the lack of step edges, as shown in Fig. 2. It is not clear whether the oriented nucleation takes place on a grain boundary or a terrace itself since both locations are essentially indistinguishable by AFM. In the case of nucleation on grain boundaries, the different behaviors observed at 100 K and 673 K can be understood as due to the much faster diffusion of the clusters at 673 K, which also drives the anisotropic aggregation of the clusters into the nanowire structures. In the case of nucleation on terraces, surface reactions between $(WO_3)_3$ and the underlying carbon substrate can take place to modulate the graphene structure and the subsequent nucleation behaviors. Such chemical interactions are supported by additional measurements, as discussed below.

We now turn to the simulation results and start with a quantitative assessment of the polarizable potential. In agreement with earlier studies,[5,32] the most stable structure of the $(WO_3)_3$ building block is the six-membered 'ring' isomer depicted in Fig. 3(a), in which the tungsten ions are fourfold coordinated with a single oxygen ion bridging them and two dangling oxygen ions in tetrahedral arrangement. The partial charges on each ion predicted by the present potential, also indicated on this figure, compare well with the reference data of ref. 5 and 32, which indicates that our model is realistic. Bond distances are also within 2% of those in the DFT geometry. Upon deposition on the HOPG substrate, this structure slightly deforms (RMSD of 0.43 Å relative to the isolated configuration), as shown in Fig. 3(b). Due to the conducting nature of the graphite substrates and its inclusion in our model, the charges vary by a few percent, especially for the atoms in closest contact with the substrate, where the variations reach about 10%.

The adsorption energy of the tungsten oxide trimer on HOPG amounts to 0.49 eV, which is much lower than the binding energy of the trimer itself (about 0.7 eV per tungsten–oxygen bond). This result is consistent with the noncovalent character of the interaction between the $(WO_3)_3$ cluster and the ideal HOPG substrate built in our model, although polarization forces play a noticeable role and contribute to about 20% of the adsorption energy.

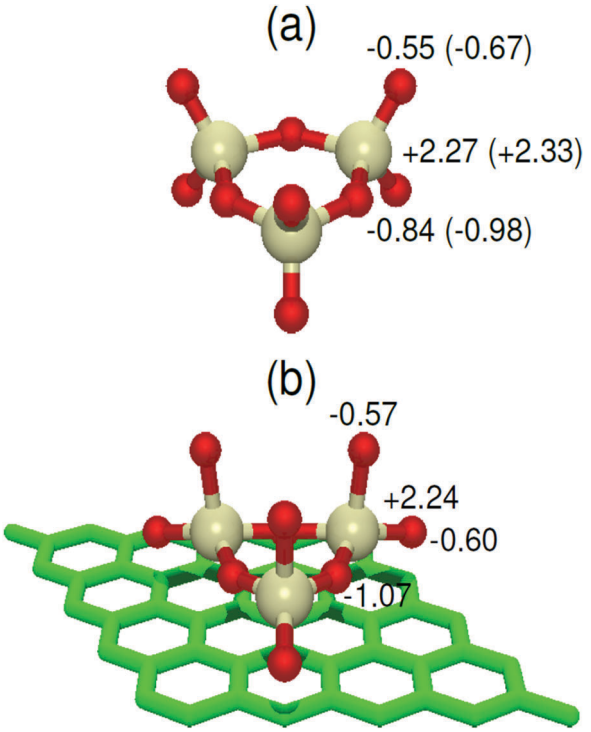

Fig. 3 Ball-and-stick representation of the most stable structure of the $(WO_3)_3$ building block, (a) in vacuum; (b) after deposition on the HOPG substrate. The effective charges on each ion are indicated, with density-functional theory reference data[32] for the isolated cluster in parentheses.

The potential was first applied to simulate the basic coalescence between two $(WO_3)_3$ monomers on the HOPG substrate, without assuming rigid building blocks or fixed charges. Here, a collision energy of 300 K was chosen, and 1000 independent trajectories were performed and stopped after 100 ps each, or if the two monomers had coalesced and formed chemical bonds at earlier times. Upon such a coalescence, a smooth friction force was added in order to relax the product to its nearby local minimum. A more accurate conjugate gradient minimization procedure was then applied in order to remove the possible residual thermal noise. Only a limited number of coalescence products was obtained from these simulations, and the statistical variety of their occurrence is depicted in Fig. 4 with three representative dimer structures. In particular, except for collisions with a large impact parameter, all events in which the two clusters approached each other within 3 Å were found to react and produce one of the structures depicted in Fig. 4, suggesting very weak barriers for reorganization and exothermic coalescence.

The building blocks generally undergo rather strong reorganization upon coalescence, the initial trimer structure being lost in the process. The lowest-energy 'inverted cage' configuration, which is also the most frequently obtained, bears some resemblance with the crystal form of WO_3. This preliminary investigation shows that atomistic rearrangements are significant upon coalescence of monomers, and confirms that it is important to relax the geometries accordingly in our main simulation of assembly processes. However, the charges do not vary by more than 10% between the monomer and the resulting dimers, which indicates that they mainly depend

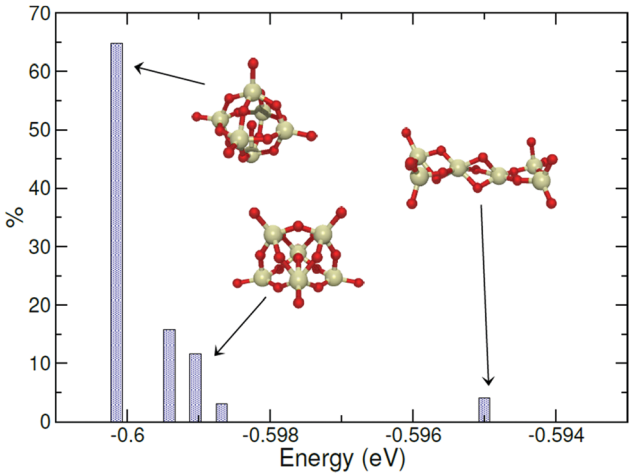

Fig. 4 Distribution of coalescence products obtained from two $(WO_3)_3$ monomers at 300 K on HOPG as a function of their binding energy. Three remarkable structures are highlighted.

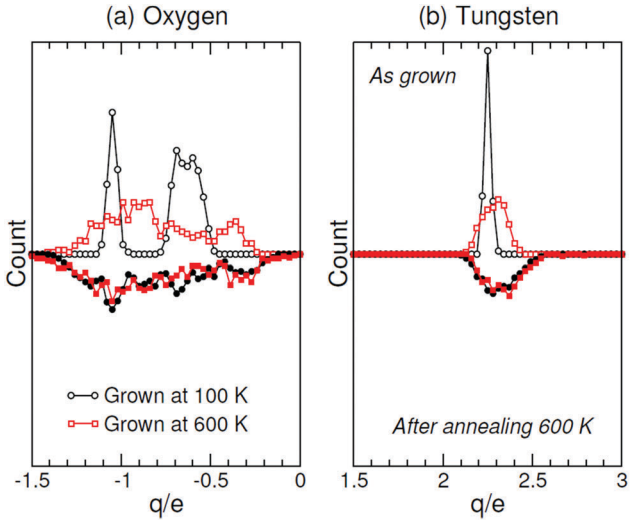

Fig. 6 Distributions of partial charges carried by the oxygen and tungsten ions in the final $[(WO_3)_3]_{100}$ assemblies grown at 100 or 600 K (upward data), and after annealing at 600 K (downward data).

on the local (fourfold) coordination of the tungsten atoms. This further justifies our approximation of constant charges to model the growth of larger assemblies.

Two series of sequential growth simulations were performed at collision energies of 100 K and 600 K, the results of which are depicted in Fig. 5. At 100 K, and as in the experiment, the assembly has a clear branched, fractal-like character that is no longer present if the assembly is grown at 600 K. As in the experiment, we also annealed the sample produced at 100 K by heating it at 600 K for 1 nanosecond, before cooling it down for 100 ps at 100 K in order to remove most of the thermal noise, treating all atomic degrees of freedom of the nanostructure without assuming rigid building blocks but keeping the partial charges fixed on all ions. The sample generated at 600 K was likewise cooled down at 100 K. The resulting structures, also represented in Fig. 5, look rather similar to one another and indicate that the ramifications are lost simply by this mild heating process.

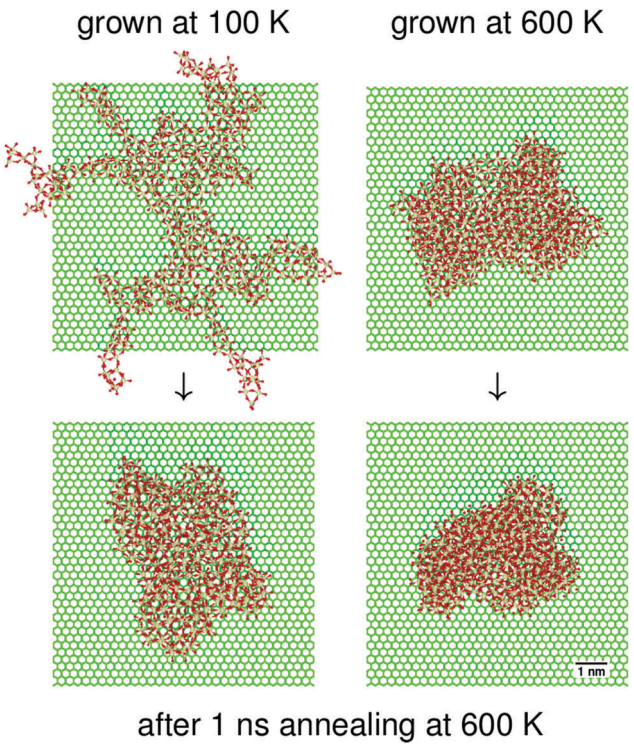

Fig. 5 Assemblies obtained from 100 units of $(WO_3)_3$ monomer clusters at 100 or 600 K collision energies (upper panels), and after annealing at 600 K (lower panels).

The structures of the assemblies at the atomic level were examined by relaxing the final configurations using the full potential with fluctuating charges. Unfortunately, the pair distribution functions happen to be poorly instructive and we turn instead to the distributions of partial charges carried by the ions and heights (coordinates perpendicular to the substrate), whose distributions are represented in Fig. 6 and 7, respectively. These distributions show some significant sensitivity to the assembly and the subsequent annealing process.

The oxide anions exhibit bimodal distributions, especially in the colder assembly, which retains most of the ordered character of the initial building block. This bimodality is associated with the different charges carried by dangling ($-0.6e$) and bridging ($-1.05e$) oxygen ions. The broadening found at 600 K and in the annealed assemblies indicates a large extent of local structural disorder. In contrast, tungsten ions are always fourfold coordinated with a charge close to their value of $+2.27e$ in the isolated monomer. Structural disorder in the hot or annealed assemblies is again reflected in the significant broadening.

The height distributions represented in Fig. 7 are also multimodal as the result of atomistic layering near the substrate. For tungsten, they expand beyond the size of the monomer, which indicates that the growth also proceeds perpendicular to the surface. This is in accordance with the results of the bimolecular collisions investigated in the previous section. The more extended

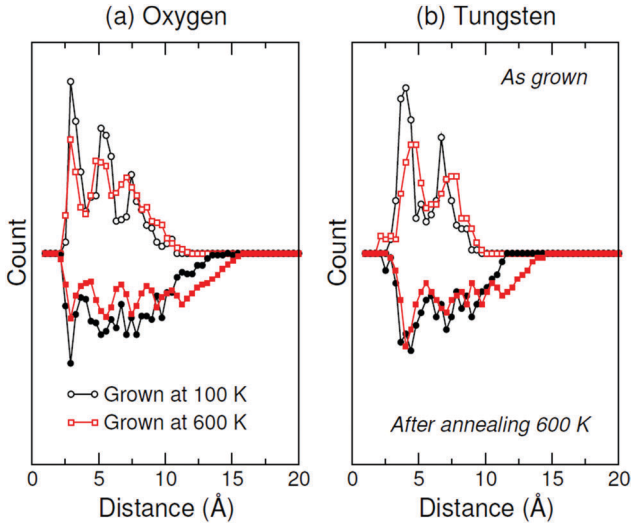

Fig. 7 Distributions of distances of the tungsten and oxygen ions in the final $[(WO_3)_3]_{100}$ assemblies grown at 100 or 600 K (upward data), and after annealing at 600 K (downward data).

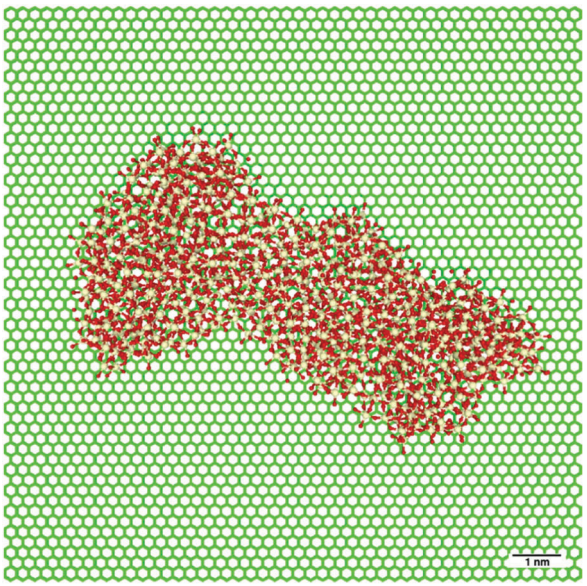

Fig. 8 Coalescence product $[(WO_3)_3]_{200}$ obtained by simulating the merging of two $[(WO_3)_3]_{100}$ nanostructures grown at 600 K and locally relaxed.

height distributions found for oxygen ions are associated with the dangling bonds pointing away from the substrate.

Upon annealing, the height distributions expand noticeably for both ion types, by about 1 Å. This expansion is consistent with the coarsening seen in Fig. 5 and is also manifested by a major decrease in the gyration radii of the nanostructures, from 317 Å to 122 Å at 100 K and from 110 Å down to 85 Å at 600 K.

To shed more light on other possible growth mechanisms, we have also explored the interaction between two small assemblies and their possible merging into a larger nanostructure by simulating their coalescence at 600 K. The growth of $(WO_3)_3$ building blocks into $[(WO_3)_3]_{100}$ at 600 K was repeated and the two products were randomly rotated and placed at 5 Å from each other and given a small negative velocity of 10^{-6} atomic units (about 2.2 m s^{-1}) to trigger coalescence. A MD simulation thermostatted at 600 K was then performed for 100 ps using the approximation of fixed charges but without any assumption regarding rigidity. The final product $[(WO_3)_3]_{200}$ thus obtained was finally cooled down to 100 K and locally minimized. It is depicted in Fig. 8.

Although the product keeps the largely disordered character of the initial assemblies, it adopts an elongated shape with lateral dimension comparable to the experimentally observed nanostructure. However, no clear orientation of the elongated nanostructure along the primitive axes of the graphite substrate is seen, a feature that is confirmed by repeating such a coalescence simulation 4 other times. This confirms the underestimation of the cluster–substrate interaction in the ideal model, which is consistent with our interpretation of growth along terraces in the experiment.

While our simulations correctly predict the small fractal-like structures for $(WO_3)_3$ clusters deposited on HOPG at 100 K caused by diffusion-limited aggregation, they do not capture their experimental preservation upon annealing, nor the long nanowires formed at 673 K, both features suggesting that the interaction is underestimated in our model, or that the assumption of an ideal HOPG substrate without any defects is unrealistic. To examine further the first possible cause of discrepancy, we first notice that the preferential orientation of nanostructures on substrates has also been observed to arise due to anisotropic lattice mismatch, as in the case of rare earth metal silicides grown on Si(110).[35] In this scenario, the nucleation sites on the two long edges of the nanowires are not energetically favored due to the high strain energy, which leads to an oriented growth along the long side. In the case where the substrate is composed of a graphene monolayer on another underlying support, lattice mismatch can also produce buckling of this upper layer, which in turn may significantly drive the sintering process.[36,37] Such strain-induced deformations of the graphitic substrates were found to be sufficiently strong to stabilize metal clusters.[37–39]

For the present system, and since bulk WO_3 has a monoclinic symmetry that is very different from the underlying graphite, some lattice mismatch between WO_3 and graphite is indeed expected. Such features were incorporated into our modeling *via* the Fourier lateral expansion in the cluster–substrate interaction, however they are clearly unsufficient to drive the growth process along the graphite primitive axes, as observed here when deposition takes place at 600 K.

As suggested above, a second possible source of discrepancy between experiments and theory is our assumption in the modeling of an ideal HOPG substrate, whereas the presence of point or line defects on the experimental HOPG substrate is very likely. In particular, if an interfacial reaction was taking place at the $(WO_3)_3$/HOPG interface, this would lead to a stronger interaction between $(WO_3)_3$ clusters and the HOPG surface and consequently, an aligned growth of nanowires. It has been shown in other systems that metal oxides on a carbonaceous support may indeed form carbides under reactive conditions.[40] To confirm this non-ideal hypothesis in the present

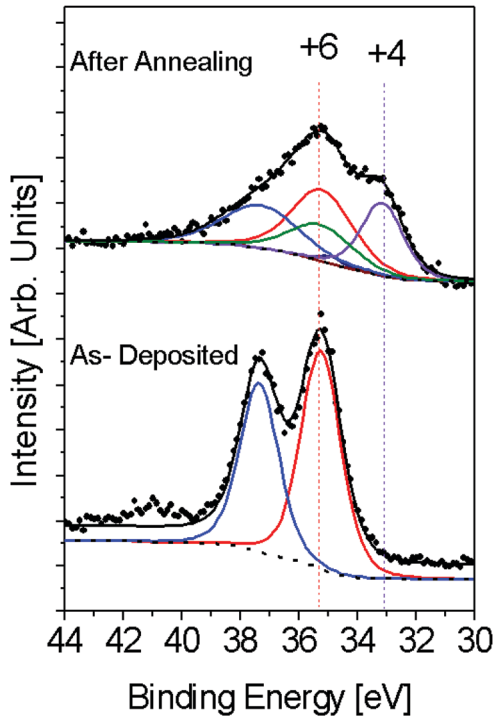

Fig. 9 *In situ* XPS spectra of the as-deposited $(WO_3)_3$ clusters and $(WO_3)_3$ clusters after *in vacuo* annealing at 673 K for 10 minutes.

experiment, additional *in situ* XPS measurements of $(WO_3)_3$ clusters on HOPG were conducted, the results being represented in Fig. 9. According to these experiments a clear reduction of tungsten is observed, as shown from the shift of the W(4f) peak to a lower binding energy after annealing. Previous studies from Li and coworkers[41] have shown little reduction of $(WO_3)_3$ supported on a graphene/Pt(111) surface up to 600 K. In our case of $(WO_3)_3$/HOPG, the bulk graphite substrate may facilitate the reduction of $(WO_3)_3$ and more precisely WO_3 itself may undergo carburization with the carbon support to form tungsten carbide. Upon heating, $(WO_3)_3$ clusters diffuse on HOPG, meanwhile some reaction with the carbon surface helps in immobilizing the $(WO_3)_3$ clusters especially in the vicinity of the reaction sites. However, we cannot verify if an interfacial buffer layer is present that can lead to epitaxial growth of the tungsten oxides on graphene. As a future study, more details of the proposed structures may be obtained *via* STM and also a comparison study on the supported graphene layer would be useful. In our follow-up work, we intend to use STM as an additional tool to further identify the nucleation sites of $(WO_3)_3$ on the HOPG surface. We believe further understanding of the reactive nature between $(WO_3)_3$ and graphite and the growth mechanism can be beneficial to the large-scale controlled growth of metal oxide nanostructures on a graphite support in a more reliable way, as an important step toward their applications in catalysis[42] and energy storage technologies.[43]

As far as computational modeling is concerned, the present potential used in the MD simulations is not reactive and cannot account for carbide formation. Neither does it describe terraces or steps that our analysis suggests play a role in anchoring the nanostructures and driving their one-dimensional growth. Despite these limitations, our coalescence simulations predict elongated nanostructures with a width that is comparable to that measured for the nanowires, thereby suggesting that the nanowires could originate from clusters containing about 100 basic $(WO_3)_3$ units.

4 Conclusions

The assembling behaviors of $(WO_3)_3$ clusters on HOPG have been studied both experimentally and theoretically. Small fractal-like aggregates were observed for $(WO_3)_3$ clusters on HOPG at 100 K, which were also predicted by simulations. Directional growth of nanowires for $(WO_3)_3$ clusters on HOPG was observed at 673 K, differing more markedly from the more compact aggregates predicted by our computational modeling. A non-ideal substrate with line defects (grain boundary) or other defects driven by surface reactions was suggested to explain such anisotropic growth, as confirmed by the additional XPS spectra showing the reduction of tungsten and the likely formation of carbides. Our modeling of the process relies on a semiempirical atomistic potential accounting for the charge transfer and polarization contributions for tungsten oxide clusters, including the effects of image charges originating from the dielectric nature of the substrate. However, a coarse-grained description of HOPG was used, neglecting any possible type of surface defects. While the model allows treating thousands of atoms on a statistical footing, further developments would be suitable notably to treat the cluster interactions more realistically in the presence of defects and account for the possible surface chemistry. A reactive potential able to account for carbide formation would be a natural but much more ambitious extension to the present work. Electronic structure calculations for small clusters on defective surfaces would be also worth considering, not only to assess their reactivity but also to parametrize the reactive potential.

Conflicts of interest

There are no conflicts to declare.

Acknowledgements

This material is based (in part) on work supported by the Office of Naval Research under grant number, ONR-MURI-N00014-15-1-2681 (KHB).

References

1 P. Poizot, S. Laruelle, S. Grugeon, L. Dupont and J. M. Tarascon, *Nature*, 2000, **407**, 496–499.
2 J. Macht and E. Iglesia, *Phys. Chem. Chem. Phys.*, 2008, **10**, 5331–5343.
3 H. Khosravian, Z. Liang, A. Uhl, M. Trenary and R. Meyer, *J. Phys. Chem. C*, 2012, **116**, 11987–11993.
4 Z. Liang, H. Khosravian, A. Uhl, R. J. Meyer and M. Trenary, *Surf. Sci.*, 2012, **606**, 1643–1648.

5 X. Huang, H. J. Zhai, B. Kiran and L. S. Wang, *Angew. Chem., Int. Ed.*, 2005, **44**, 7251–7254.
6 O. Bondarchuk, X. Huang, J. Kim, B. D. Kay, L. S. Wang, J. M. White and Z. Dohnalek, *Angew. Chem., Int. Ed.*, 2006, **45**, 4786–4789.
7 Y. K. Kim, R. Rousseau, B. D. Kay, J. M. White and Z. Dohnalek, *J. Am. Chem. Soc.*, 2008, **130**, 5059.
8 J. Kim, B. D. Kay and Z. Dohnalek, *J. Phys. Chem. C*, 2010, **114**, 17017–17022.
9 S. Pomp, D. Kuhness, G. Barcaro, L. Sementa, V. Mankad, A. Fortunelli, M. Sterrer, F. P. Netzer and S. Surnev, *J. Phys. Chem. C*, 2016, **120**, 7629–7638.
10 L. Ma, M. Denk, D. Kuhness, S. Surnev, V. Mankad, G. Barcaro, A. Fortunelli and F. P. Netzer, *Surf. Sci.*, 2015, **640**, 96–103.
11 Z. J. Li, Z. R. Zhang, Y. K. Kim, R. S. Smith, F. Netzer, B. D. Kay, R. Rousseau and Z. Dohnalek, *J. Phys. Chem. C*, 2011, **115**, 5773–5783.
12 M. Shimonaka, Y. Nakamura, J. Kikkawa and A. Sakai, *Surf. Sci.*, 2014, **628**, 82–85.
13 B. Kiran, A. K. Kandalam, R. Rallabandi, P. Koirala, X. Li, X. Tang, Y. Wang, H. Fairbrother, G. Gantefoer and K. Bowen, *J. Chem. Phys.*, 2012, **136**, 024317.
14 P. J. Kowalczyk, O. Mahapatra, D. N. McCarthy, W. Kozlowski, Z. Klusek and S. A. Brown, *Surf. Sci.*, 2011, **605**, 659–667.
15 Y. Nakamura, F. Kagawa, K. Kasai, Y. Mera and K. Maeda, *Appl. Phys. Lett.*, 2004, **85**, 5242–5244.
16 P. Scheier, B. Marsen, M. Lonfat, W.-D. Schneider and K. Sattler, *Surf. Sci.*, 2000, **458**, 113–122.
17 J. M. Notestein, E. Iglesia and A. Katz, *J. Am. Chem. Soc.*, 2004, **126**, 16478–16486.
18 N. E. Thornburg, A. B. Thompson and J. M. Notestein, *ACS Catal.*, 2015, **5**, 5077–5088.
19 C. A. Roberts, D. Prieto-Centurion, Y. Nagai, Y. F. Nishimura, R. D. Desautels, J. van Lierop, P. T. Fanson and J. M. Notestein, *J. Phys. Chem. C*, 2015, **119**, 4224–4234.
20 S. Liu, J. M. Tan, A. Gulec, L. A. Crosby, T. L. Drake, N. M. Schweitzer, M. Delferro, L. D. Marks, T. J. Marks and P. C. Stair, *Organometallics*, 2017, **36**, 818–828.
21 S. A. Claridge, A. W. Castleman, S. N. Khanna, C. B. Murray, A. Sen and P. S. Weiss, *ACS Nano*, 2009, **3**, 244–255.
22 X. Tang, D. Bumueller, A. Lim, J. Schneider, U. Heiz, G. Ganteför, D. H. Fairbrother and K. H. Bowen, *J. Phys. Chem. C*, 2014, **118**, 29278–29286.
23 K. A. Wepasnick, X. Li, T. Mangler, S. Noessner, C. Wolke, M. Grossmann, G. Gantefoer, D. H. Fairbrother and K. H. Bowen, *J. Phys. Chem. C*, 2011, **115**, 12299–12307.
24 F. Calvo, K. Bowen and X. Tang, *J. Phys. Chem. C*, 2014, **118**, 1306–1317.
25 F. Calvo, *Phys. Rev. B: Condens. Matter Mater. Phys.*, 2003, **67**, 161403.
26 K. Ohno, *Theor. Chim. Acta*, 1964, **2**, 219–227.
27 W. A. Steele, *Surf. Sci.*, 1973, **36**, 317–352.
28 W. L. Jorgensen, D. S. Maxwell and J. Tirado-Rives, *J. Am. Chem. Soc.*, 1996, **118**, 11225–11236.
29 B. S. González, J. Hernández-Rojas, J. Bretón and J. M. G. Llorente, *J. Phys. Chem. C*, 2007, **111**, 14862–14869.
30 F. Calvo, *Phys. Rev. A: At., Mol., Opt. Phys.*, 2006, **74**, 043202.
31 S. W. Rick, S. J. Stuart and B. J. Berne, *J. Chem. Phys.*, 1994, **101**, 6141–6156.
32 S. Li and D. A. Dixon, *J. Phys. Chem. A*, 2006, **110**, 6231–6244.
33 X. Li, K. A. Wepasnick, X. Tang, Y. Wang, K. H. Bowen, D. H. Fairbrother and G. Gantefoer, *J. Vac. Sci. Technol., B: Nanotechnol. Microelectron.: Mater., Process., Meas., Phenom.*, 2012, **30**, 031806.
34 M. Schmidt, N. Kébaïli, A. Lando, S. Benrezzak, L. Baraton, P. Cahuzac, A. Masson and C. Bréchignac, *Phys. Rev. B: Condens. Matter Mater. Phys.*, 2008, **77**, 205420.
35 Y. Chen, D. A. A. Ohlberg and R. S. Williams, *J. Appl. Phys.*, 2002, **91**, 3213–3218.
36 E. Loginova, S. Nie, K. Thurmer, N. C. Bartelt and K. F. McCarty, *Phys. Rev. B: Condens. Matter Mater. Phys.*, 2009, **80**, 085430.
37 E. Soy, Z. Liang and M. Trenary, *J. Phys. Chem. C*, 2015, **119**, 24796–24803.
38 M. A. Zhou, A. H. Zhang, Z. X. Dai, Y. P. Feng and C. Zhang, *J. Phys. Chem. C*, 2010, **114**, 16541–16546.
39 A. T. N'Diaye, S. Bleikamp, P. J. Feibelman and T. Michely, *Phys. Rev. Lett.*, 2006, **97**, 215501.
40 J. Ma and S. G. Zhu, *Int. J. Refract. Met. Hard Mater.*, 2010, **28**, 623–627.
41 Z. Li, Z. Fang, M. S. Kelley, B. D. Kay, R. Rousseau, Z. Dohnalek and D. A. Dixon, *J. Phys. Chem. C*, 2014, **118**, 4869–4877.
42 B. Weng, J. Wu, N. Zhang and Y.-J. Xu, *Langmuir*, 2014, **30**, 5574–5584.
43 S. A. Pervez, D. Kim, C.-H. Doh, U. Farooq, H.-Y. Choi and J.-H. Choi, *ACS Appl. Mater. Interfaces*, 2015, **7**, 7635–7643.

